

Article

Computational Insight into Defective Boron Nitride Supported Double-Atom Catalysts for Electrochemical Nitrogen Reduction

Rong Cao ^{1,2}, Jie-Zhen Xia ^{1,2} and Qi Wu ^{1,2,3,*}¹ School of Science, Tibet University, Lhasa 850000, China² Institute of Oxygen Supply, Center of Tibetan Studies (Everest Research Institute), Tibet University, Lhasa 850000, China³ Key Laboratory of Cosmic Rays, Tibet University, Ministry of Education, Lhasa 850000, China

* Correspondence: wuqi@utibet.edu.cn

Abstract: Designing highly selective and efficient double-atom electrocatalysts (DACs) is essential for achieving a superior nitrogen-reduction reaction (NRR) performance. Herein, we explored the defective boron nitride-supported cage-like double-atom catalysts to rummage the qualified NRR catalysts. Based on a systematic evaluation of the stability, N₂ adsorption, NRR selectivity and activity of 10 DACs of TM₁-TM₂@V_B-BN, we predicted Ru-Ti@V_B-BN to be the NRR candidate with a limiting potential of −0.40 V. Compared to the corresponding single-atom catalysts, the introduction of Ti/Mo modulates the *d*-band center of the active metal atom, which improves the NRR performance. Moreover, the magnetic Ru-Ti dimer can facilitate the transfer of charge to molecular N₂, ensuring a significant activation of the inert N≡N bond. This research not only opens up new avenues for designing boron nitride-supported DACs for NRR, but also deepens the understanding of DACs in N₂ activation.

Keywords: boron nitride monolayer; dual-atom catalysts; NRR; DFT

Citation: Cao, R.; Xia, J.-Z.; Wu, Q. Computational Insight into Defective Boron Nitride Supported Double-Atom Catalysts for Electrochemical Nitrogen Reduction. *Catalysts* **2022**, *12*, 1404. <https://doi.org/10.3390/catal12111404>

Academic Editors: Zhongzhe Wei and Yutong Gong

Received: 24 October 2022

Accepted: 8 November 2022

Published: 10 November 2022

Publisher's Note: MDPI stays neutral with regard to jurisdictional claims in published maps and institutional affiliations.



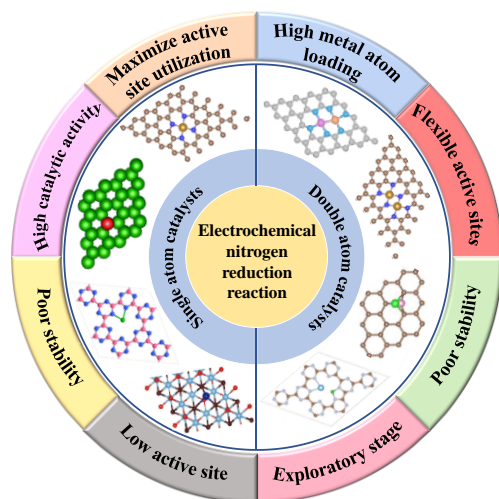
Copyright: © 2022 by the authors. Licensee MDPI, Basel, Switzerland. This article is an open access article distributed under the terms and conditions of the Creative Commons Attribution (CC BY) license (<https://creativecommons.org/licenses/by/4.0/>).

1. Introduction

Ammonia (NH₃) plays an extremely important role in the modern agriculture and chemical industry [1,2]. Currently, industrial NH₃ synthesis requires the reduction of nitrogen (N₂) to NH₃ with the help of iron-based catalysts at a high temperature (300–500 °C) and high pressure (150–300 atm) by means of the Haber–Bosch process [3,4]. Inspired by the biological nitrogen fixation occurring under mild conditions, the electrochemical nitrogen reduction reaction (NRR) has attracted great attention as a promising NH₃ production method [5,6]. However, efficient N₂ reduction has been proven to be extremely tough owing to the chemically inert N≡N triple bond with a high bond energy of 940.95 kJ mol^{−1} [7,8]. Meanwhile, most catalysts exhibit poor selectivity toward NRR, mainly due to the existence of a competing hydrogen evolution reaction (HER) in aqueous solution and a low overpotential of HER [9–12]. To overcome these challenges, searching for high-performance catalysts with low working overpotential, good stability and high selectivity remains a highly rewarding task.

As an emerging class of atomically dispersed catalysts, single-atom catalysts (SACs) have been widely used in NRR due to their high atom utilization and excellent catalytic performance [13]. However, the low stability of the anchoring individual metal atom on the substrate material makes them prone to agglomerate during the reaction [14]. In addition, NRR involves multiple reaction steps, and it is difficult for a single active site to simultaneously regulate the adsorbed intermediates, resulting in its low Faradaic efficiency and NH₃ yield [15]. The introduction of bimetallic pairs can effectively solve this problem. For example, Chen et al. [16] systematically explored the performance of double transition metals (TMs) anchored on C₂N (TM₂-C₂N) for NRR by first principles calculations. In contrast with the performance on corresponding SACs (TM₁-C₂N), the studies highlighted

that $\text{Mn}_2\text{-C}_2\text{N}$ favors NH_3 electrosynthesis and that the predicted overpotential can reach -0.23 V. Zhang et al. [17] proposed double Fe anchored on N-doped graphene ($\text{Fe}_2\text{N}_4@\text{NG}$) as the most excellent NRR catalyst, with a relatively low overpotential of -0.32 V. It is evident that DACs emerge as promising NRR catalysts, benefiting from their higher metal-atom loading and flexible active sites. The comparative information of SACs and DACs catalysts is shown in Scheme 1.



Scheme 1. Representative structures of single- and double-atom catalysts reported in the past five years and their corresponding advantages and disadvantages.

In atomic catalysts, appropriate substrates also play major roles by stabilizing and dispersing DACs at a specific site. Boron nitride (BN) nanosheets are widely used in the field of energy storage due to their high chemical stability and unique physical and chemical properties [18–20]. It has been proven that boron vacancies (V_B) are easier to form in h-BN sheets than nitrogen vacancies (V_N). Moreover, the h-BN sheets containing V_B have been widely used as substrates to support metal atoms, which serve as a promising catalyst for the NRR process. Zhao et al. [21] showed that single Mo anchored on the defective BN exhibited high catalytic activity, along with extremely low overpotential (-0.19 V). However, the study of the DACs based on defective BN remains in its infant stage. Recently, researchers have designed DACs imitating the configuration of cage-like nitrogenase active centers, such as Fe-TM double atoms anchored on graphene [22,23]. They have been reported to not only show superior NRR activity, but also effectively retard the agglomeration of metal atoms and facilitate electron transfer between N_2 and the graphene surface. It is evident that the cage-like double metal active centers have a unique application potential in NRR catalytic reactions. These pioneering works in fabricating cage-like DACs are of critical importance for the expansion of broad electrochemical reactions applying BN as supported catalysts.

In this work, we adopted four commonly used transition metal atoms (TM = Ti, Fe, Mo and Ru) and designed cage-like diatomic TMs N_2 -fixing catalysts on defective BN ($V_B\text{-BN}$). The justification for choosing these TMs lies in the fact that numerous studies have shown that Fe, Mo and Ru could act as catalytic centers for NRR [24–27]. More recently, Xia et al. predicted that Ti doping could improve the stability of defective BN and enhance the NRR performance compared with the pristine BN [28]; hence, we adopted the earth-abundant transition metal Ti to anchor on BN for NRR. Based on density functional theory (DFT), we systematically evaluated the stability of the substrate, N_2 adsorption, NRR selectivity and activity of 10 $\text{TM}_1\text{-TM}_2@V_B\text{-BN}$ candidates. Three promising DACs were proposed ($\text{Ru-Mo/Ru/Ti}@V_B\text{-BN}$) as excellent NRR catalysts, and the best one was predicted to be $\text{Ru-Ti}@V_B\text{-BN}$, with a low overpotential of -0.40 V, along the enzymatic pathway. We also performed an in-depth interaction mechanism and electronic structure analysis to

reveal the inherent regularity of catalytic activity. Our work not only enriches existing BN-supported NRR electrocatalysts, but also offers a feasible clue for the experimental explorations ahead.

2. Results and Discussion

2.1. Structural and Electronic Properties of $TM_1-TM_2@V_B-BN$

Defective BN (V_B-BN) with one B atom removed was adopted as the substrate to anchor the transition metal atoms ($TM = Ti, Fe, Mo$ and Ru). Then 10 $TM_1-TM_2@V_B-BN$ structures were locked by embedding a cage-like TM dimer (dopant pairs) in the V_B-BN substrate adjacent to the B vacancy. All the optimized structures of the $TM_1-TM_2@V_B-BN$ system are plotted in Figure 1a and Supplementary Figure S2.

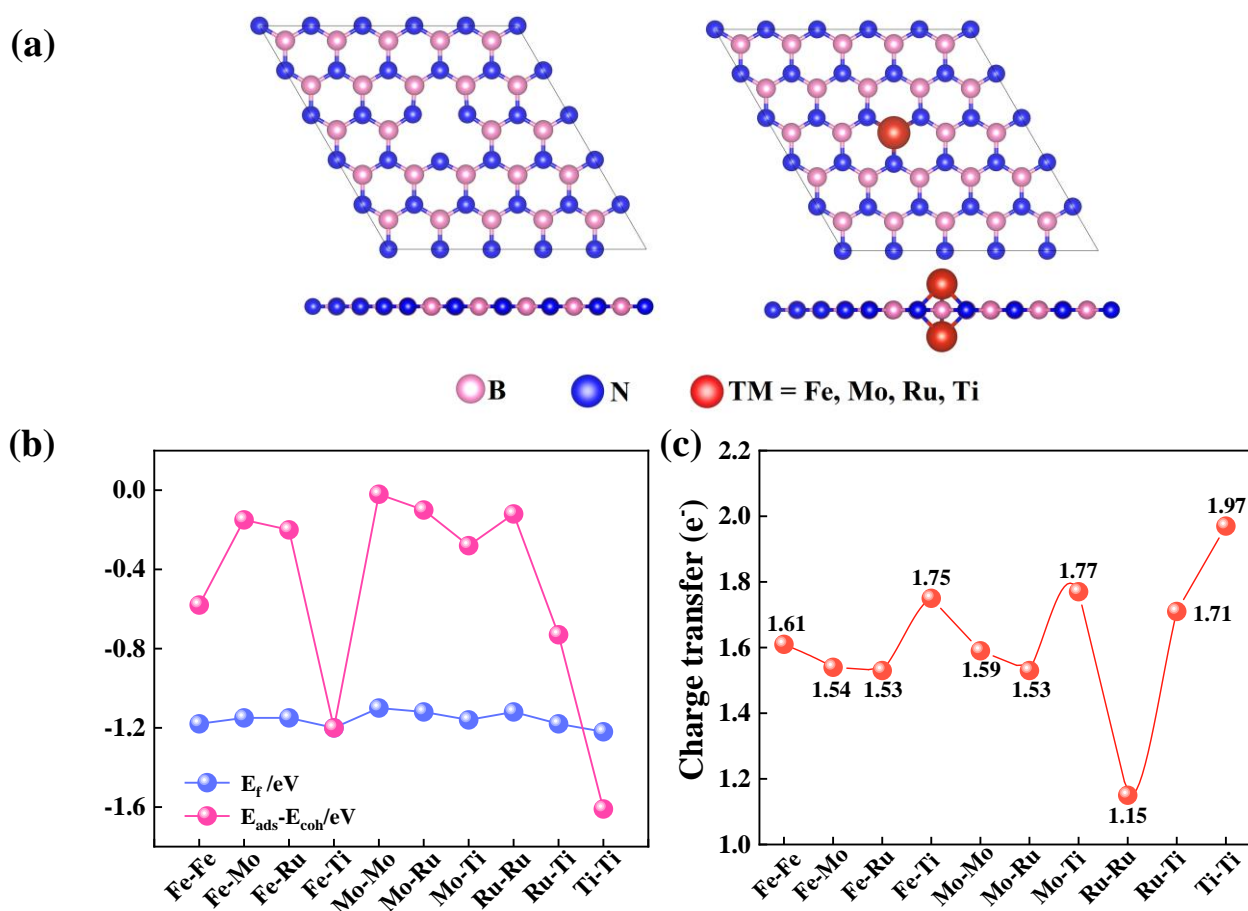


Figure 1. (a) Schematic configurations of $TM_1-TM_2@V_B-BN$. (b) Calculated formation energy and the difference between the adsorption energy and cohesive energy of the $TM_1-TM_2@V_B-BN$ systems. (c) Charge transfer from the TM pair to the V_B-BN substrate.

To verify the experimental synthetic feasibility, we evaluated the structural and thermodynamic stability of all $TM_1-TM_2@V_B-BN$ candidates. As Supplementary Figure S2 shows, all the optimized DACs maintain their planar structures with the cage-like TM dopants protruding out of the BN monolayer, implying high structural stabilities. The formation energy of $TM_1-TM_2@V_B-BN$ was calculated based on the formula as follows:

$$E_f = (E_{\text{catalysts}} - x\mu_B - y\mu_N - \mu_{TM1} - \mu_{TM2}) / n$$

where $E_{\text{catalysts}}$ is the total energies of the TM-doped BN; μ_B , μ_N , μ_{TM1} and μ_{TM2} are the chemical potentials of single B, N and TM atoms in their bulk structure; n is the total number of atoms in $TM_1-TM_2@V_B-BN$; and x and y are the number of B and N atoms in the

substrate, respectively. The difference between the adsorption energies of the TM atoms and the cohesive energy of the corresponding base species can be used to assess whether the metal can be stably anchored on the base material or aggregates to form clusters.

$$E_{\text{ads}} = (E_{\text{catalysts}} - E_{\text{slab}} - E_{\text{TM1}} - E_{\text{TM2}})/2$$

$$E_{\text{coh}} = [(E_{\text{bulk(TM1)}} - E_{\text{TM1}}) + (E_{\text{bulk(TM2)}} - E_{\text{TM2}})]/2$$

where $E_{\text{catalysts}}$ and E_{slab} are the total energies of the TM-doped BN and supports; and E_{TM1} , E_{TM2} , $E_{\text{bulk(TM1)}}$ and $E_{\text{bulk(TM2)}}$ are the energies of the isolated atom and the single TM atoms in their bulk structure. The calculated corresponding energies can be found in Figure 1b and Supplementary Table S1. As revealed in Figure 1b, it is interesting to note that all the E_f and $E_{\text{ads}} - E_{\text{coh}}$ values are well below zero, indicating the high stability of the dopant TM atoms.

With respect to DACs, the insertion of dopant TM pairs leads to the change of the local environment and electronic property [29]. We hence examined the TMs–substrate interactions by performing the Bader charge analysis. From Figure 1c and Supplementary Table S2, we found significant electron transfer from the TM atoms to the V_B -BN substrate, ranging from 1.15 |e| to 1.97 |e|, which supports the strong interactions between the TM atoms and the V_B -BN substrate. However, the electronegativity also affects the electron transfer of the TM pairs embedded in V_B -BN substrate. For instance, the Ti atom, which has the smallest electronegativity (1.54 e) among all the candidate metal atoms, exhibits a strong ability to bind to the substrate, accompanying large amounts of electron transfer. However, for Ru (2.2 e for electronegativity), the electron transfer is not promising among all the candidates.

2.2. N_2 Adsorption and Selectivity on TM_1 - TM_2 @ V_B -BN

Firstly, the capture and adsorption of N_2 are prerequisites, meaning that the Gibbs free energy change (ΔG) for stable N_2 adsorption should be lower than 0 eV ($\Delta G(*N_2) < 0$) [30]. Considering the adsorption of N_2 , the heteronuclear and homonuclear DACs provide two adsorption sites and one adsorption site, respectively. Consequently, we totally considered 16 adsorption configurations and calculated the $\Delta G(*N_2)$ values of N_2 terminated on TM_1 - TM_2 @ V_B -BN in end-on/side-on manners (see Table 1). Moreover, the NRR catalyst should effectively inhibit competitive HER, which is also an important indicator of the catalyst's efficiency. The surface of catalysts must provide enough active sites for N_2 activation, so as to facilitate the subsequent reactions. A stronger adsorption activity of the N_2 molecule is essential for high NRR selectivity, which ensures that the catalyst selectively adsorbs N_2 molecular prior to H [31,32]. As a matter of convenience, we determined the catalytic selectivity of TM_1 - TM_2 @ V_B -BN through a comparison of the adsorption free energies of the $*N_2$ and $*H$ atom.

As Figure 2a displays below, all structures have a negative $\Delta G(*N_2)$, indicating that the N_2 molecule can be stably anchored on the catalyst for subsequent hydrogenation reactions. For all the DACs, the capture of N_2 prefers side-on mode with lower $\Delta G(*N_2)$ than that of end-on configurations. Fe-Fe@ V_B -BN was not displayed, since it has the most negative $\Delta G(*N_2)$, at -2.12 eV, and would be detrimental to production and desorption of NH_3 . For catalyst selectivity, TM_1 - TM_2 @ V_B -BN in the lower-right region of Figure 2a is favorable for NRR. Most of the dopant pairs decorated V_B -BN are within the area of $\Delta G(*N_2) < \Delta G(*H)$, with the exception of Ti-Mo and Ti-Ru (see Table 1). Our results imply that these candidates are more inclined to adsorb $*N_2$ and that the adsorption of $*N_2$ is stronger than that of $*H$. This means that the coverage of N_2 molecules on the surface of these catalysts is relatively large; that is to say, these candidates show high NRR selectivity. However, the candidate Ti-Mo/Ti-Ru@ V_B -BN displayed lower NRR activity when N_2 molecules were adsorbed in end-on mode compared to HER, as they were deleted from the ensemble of catalysts candidates.

Table 1. Calculated free energy changes for *H ($\Delta G(^*H)$) and *N_2 ($\Delta G(^*N_2)$) on 16 TM_1 - $TM_2@V_B$ -BN catalysts. TM_1 is the adsorption site for N_2 .

	Fe-Fe	Fe-Mo	Fe-Ru	Fe-Ti	Mo-Mo	Mo-Ru
$\Delta G(^*H)$	-0.78	-0.73	-0.54	-0.81	-0.78	-0.81
$\Delta G(^*N_2)/\text{end-on}$	-1.46	-1.29	-1.31	-1.44	-1.23	-0.99
$\Delta G(^*N_2)/\text{side-on}$	-2.12	-1.06	-0.96	-1.26	-1.36	-1.1
	Mo-Ti	Ru-Ru	Ru-Ti	Ti-Ti	Ti-Ru	
$\Delta G(^*H)$	-0.80	-0.55	-0.62	-0.93	-0.87	
$\Delta G(^*N_2)/\text{end-on}$	-1.20	-1.12	-1.20	-0.40	-0.78	
$\Delta G(^*N_2)/\text{side-on}$	-1.31	-0.68	-0.89	-1.33	-0.90	
	Ti-Mo	Ti-Fe	Ru-Mo	Ru-Fe	Mo-Fe	
$\Delta G(^*H)$	-1.00	-0.89	-0.57	-0.60	-0.87	
$\Delta G(^*N_2)/\text{end-on}$	-0.88	-0.98	-1.05	-1.38	-1.19	
$\Delta G(^*N_2)/\text{side-on}$	-1.07	-1.12	-0.70	-0.83	-1.23	

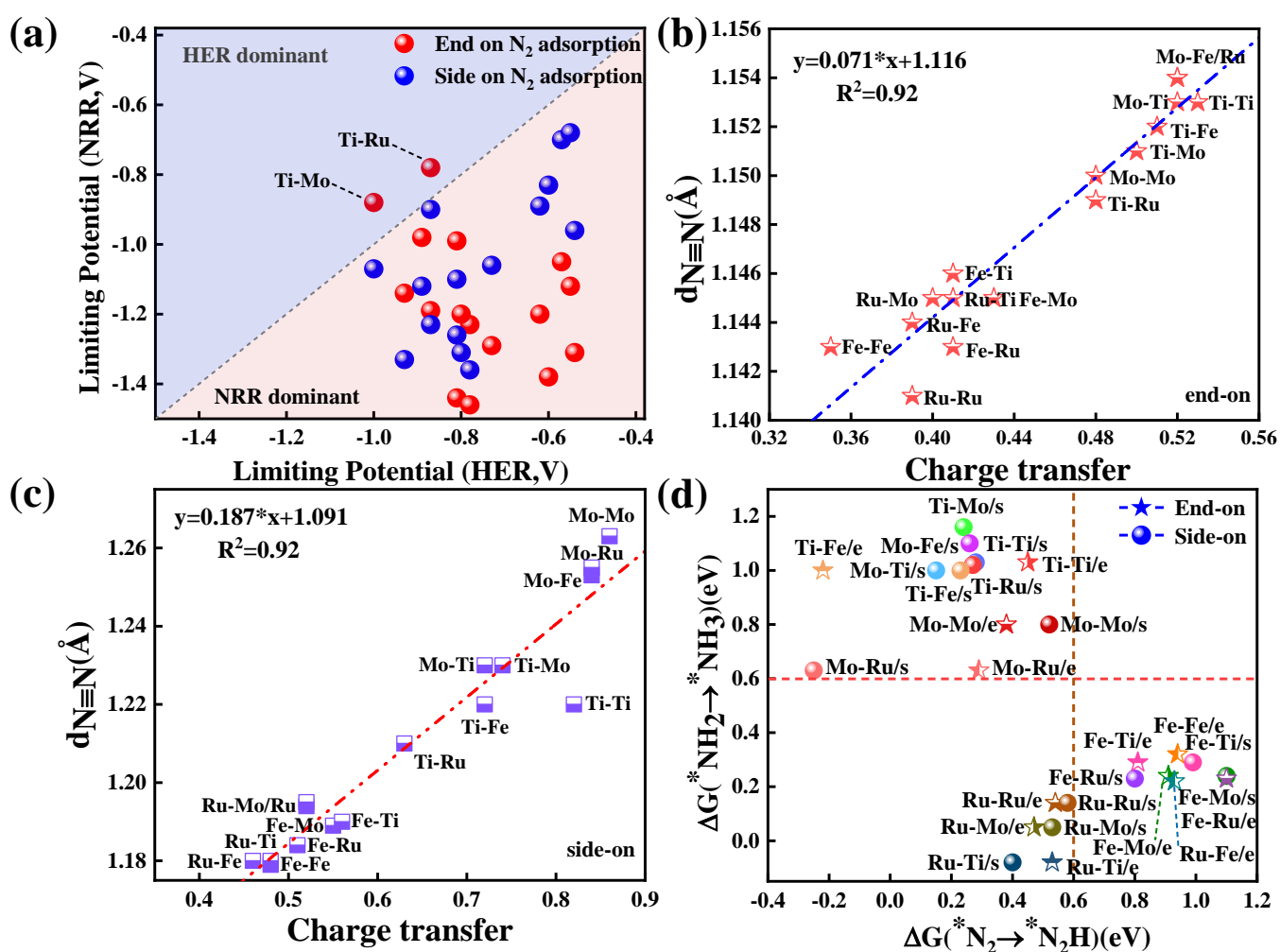


Figure 2. (a) Comparison of the HER limiting potentials and NRR limiting potentials via side-on and end-on mode. The relationship between the N-N bond length (d_{N-N}) and the charge *N_2 gained from the TM_1 - $TM_2@V_B$ -BN substrate through (b) end-on and (c) side-on pattern. (d) Free energy change of the first hydrogenation step ($\Delta G(^*N_2 \rightarrow ^*N_2H)$) and the last hydrogenation step ($\Delta G(^*NH_2 \rightarrow ^*NH_3)$) for different DACs.

We also measured the N-N bond length ($d_{\text{N-N}}$) and the charge N_2 gained from the base material, and the relationships between the two are shown in Figure 2b,c. Interestingly, Figure 2b,c show that the greater the charge accumulation on N_2 , the longer the N-N bond length. Upon N_2 adsorption, $d_{\text{N-N}}$ in terminated N_2 is elongated and within the range of 1.14–1.15 Å (end-on)/1.18–1.26 Å (side-on) (vs 1.12 Å in free gas phase), implying that $\text{TM}_1\text{-TM}_2@V_{\text{B}}\text{-BN}$ candidates are effective in the activation of N_2 molecule. In addition, these data also indicate that the bond length of N_2 adsorbed in the side-on configuration is significantly longer than that in the end-on configuration. This can be attributed to the fact that when the TM adsorbs N_2 in a side-on configuration, both N atoms will bond with the TM and will mutual repulsion, resulting in a longer N-N bond. Figure 2b also shows that the catalysts transferred 0.35–0.52 |e| to N_2 adsorbed through end-on mode. In contrast, our results indicate that N_2 adsorbed through side-on mode can gain more charge (0.46–0.86 |e|) from the catalysts, thus activating $\text{N}\equiv\text{N}$ triple bond more effectively (see Supplementary Table S3).

2.3. Catalytic Activity of $\text{TM}_1\text{-TM}_2@V_{\text{B}}\text{-BN}$

After clarifying the N_2 adsorption strength and selectivity, we further studied the catalytic activity of DACs. Generally, the inevitable first hydrogenation step ($^*\text{N}_2 + \text{H}^+ + \text{e}^- \rightarrow ^*\text{N}_2\text{H}$) requires a large energy consumption to break the inert $\text{N}\equiv\text{N}$ triple bond and, hence, induces a positive ΔG . Moreover, the last hydrogenation reaction ($^*\text{NH}_2 + \text{H}^+ + \text{e}^- \rightarrow ^*\text{NH}_3$) is usually achieved with an uphill in ΔG due to the strong combination between the $^*\text{NH}_2$ species and TM atoms [33]. Therefore, we set the Gibbs free energy change of the first ($\Delta G_{^*\text{N}_2 \rightarrow ^*\text{N}_2\text{H}}$) and the last hydrogenation step ($\Delta G_{^*\text{NH}_2 \rightarrow ^*\text{NH}_3}$) at less than 0.6 eV as a criterion to ensure a low limiting potential. This criterion is half the rate-determining step of pristine BN (1.20 eV), which is superior to the commonly used metal catalyst Ru (0001) (0.98 eV).

As portrayed in Figure 2d, the $\text{TM}_1\text{-TM}_2@V_{\text{B}}\text{-BN}$ catalysts in the upper-left region, corresponding to the structures in the upper-right panel of Figure 2b or Figure 2c, can meet our restricted value only for the first hydrogenation step. Obviously, these catalysts exhibit a significant activation of the N_2 molecule, which makes the first hydrogenation step easier to occur. However, too-strong N_2 adsorption would lead to the unfavorable formation and desorption of NH_3 ; hence, the ΔG values of the last hydrogenation reaction for these systems deviate from our criterion (0.6 eV). In contrast, those catalysts located in the bottom-left corner of Figure 2b or Figure 2c require a higher energy demand in the formation of $^*\text{N}_2 \rightarrow ^*\text{N}_2\text{H}$. Those catalysts are finally found in the bottom-right area of Figure 2d and ruled out at this step. Consequently, only the candidates located in the bottom-left area with moderate N_2 adsorption strengths can reach the criteria. Ru-Mo@ $V_{\text{B}}\text{-BN}$, Ru-Ru@ $V_{\text{B}}\text{-BN}$ and Ru-Ti@ $V_{\text{B}}\text{-BN}$ show superior NRR activity, along with the least energy requirements for both the first and last protonation process. In conclusion, Ru-Mo@ $V_{\text{B}}\text{-BN}$, Ru-Ru@ $V_{\text{B}}\text{-BN}$ and Ru-Ti@ $V_{\text{B}}\text{-BN}$ are considered to be potential NRR catalysts, and they are discussed in the following sections. Other structures' values of ΔG for the two hydrogenation steps are listed in Supplementary Table S4, respectively.

2.4. Activation Mechanisms of N_2 on Ru-Mo/Ru/Ti@ $V_{\text{B}}\text{-BN}$

To reveal the active origin of NRR, we analyzed the interactions between metal active sites and reaction intermediates. As shown in Figure 3, we took the most promising candidates, Ru-Mo@ $V_{\text{B}}\text{-BN}$, Ru-Ru@ $V_{\text{B}}\text{-BN}$ and Ru-Ti@ $V_{\text{B}}\text{-BN}$, as the typical systems for further analysis. Their charge-density-difference plots and key bond length are displayed in Figure 3. Remarkably, N_2 tends to interact with the top Ru atom; hence, we mainly analyzed the electronic transfer situation between the Ru atom and N_2 . Obviously, Figure 3 reveals a significant charge redistribution, which mainly occupies the antibonding orbitals of the adsorbed N_2 , leading to the elongation of the N-N bond. Moreover, $d_{\text{N-N}}$ (1.18/1.19 Å) of N_2 adsorbed in the side-on mode is longer than that in the end-on mode (1.14 Å), and this resonates with the amount of charge transfer between the TM atom and $^*\text{N}_2$.

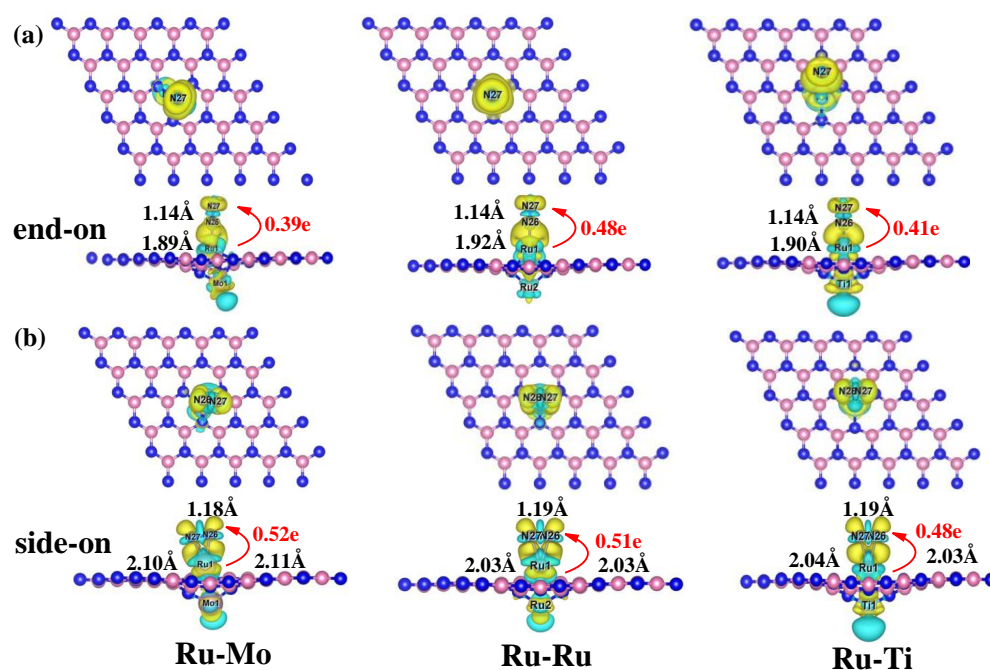


Figure 3. Optimized structures and charge density differences of *N_2 on Ru-Mo@ V_B -BN, Ru-Ru@ V_B -BN and Ru-Ti@ V_B -BN catalysts for (a) end-on and (b) side-on configurations. The key bond lengths are also given.

In addition, we also compared the activation effect of the TM dimer on N_2 by considering a model of single-atom Ru anchored on V_B -BN. Similarly, N_2 molecules are adsorbed on the Ru active site in two manners, and the charge density differences and Bader charge analysis were also analyzed (see Supplementary Figure S3). For Ru@ V_B -BN, the single Ru atom donates $0.34|e|$ and $0.28|e|$ to *N_2 , which is less than the amount of charge transferred in the case of Ru-Mo/Ru/Ti@ V_B -BN. Consequently, our simulations confirm that N_2 adsorbed on the DACs can gain more charge from the catalysts, thus activating the inert $N\equiv N$ bond more effectively.

To uncover the underlying mechanism of N_2 activation, the partial density of states (PDOS) of bare and N_2 -terminated Ru-Mo/Ru/Ti catalysts was analyzed. Particularly, Figure 4a shows four characteristic orbitals, namely $2\sigma^*$, 1π , 3σ and $1\pi^*$, in free N_2 molecular within the range of $-5 \sim 7$ eV. As shown in Figure 4d–f, the electrons were obviously transferred from the occupied Ru $4d$ orbital to the empty π^* orbital of N_2 after N_2 adsorption. As a result, the antibonding π^* orbitals of adsorbed *N_2 on these three catalysts reveal a significant down-shifting in comparison with isolated N_2 molecular. Correspondingly, the unoccupied d orbitals of the Ru atom accepted the electrons from *N_2 , forming the Ru-N bonding state to strengthen the N_2 capture, as evidenced by the evident hybridization between Ru- $4d$ and N- $2p$ orbitals around the Fermi level. In addition, the d -band centers (ϵ_d) of the active Ru sites before the adsorption of N_2 molecules for the three catalysts were also calculated and marked in Figure 4. It can be seen from Figure 4c that the Ru-Ti structure is easier to adsorb and activate N_2 because its ϵ_d is closer to the Fermi level. Compared with the homonuclear diatomic catalyst Ru-Ru@ V_B -BN, the introduction of coordinating metal atoms Ti and Mo affects the ϵ_d of Ru atom to different degrees. Interestingly, the Ti atom causes Ru to obtain a higher ϵ_d , which can be attributed to the higher electronegativity of Ti, hence making the activation of Ru-Ti@ V_B -BN easier for N_2 . For Ru@ V_B -BN, we also calculated its d -band center (see Supplementary Figure S4). In contrast, since the second metal atom on the surface also interacts with the adsorbate, the d orbitals of both metal atoms are involved to some extent. Their activities can be reasonably described by the central location of the PDOS corresponding to the d state. It can be seen from the numerical value that the diatomic catalyst has higher catalytic activity. Recently, Guo

et al. suggested that the magnetic moment, μ_B , of a metal surface plays an important role in NH_3 synthesis [34]. Based on this, we investigated the μ_B of the Ru active site in Ru-Mo/Ru/Ru/Ti@ V_B -BN systems (see Supplementary Table S5). The calculated μ_B values for Ru atoms in Ru-Mo/Ru/Ru/Ti@ V_B -BN catalysts are 1.55, 1.08 and 1.60, respectively, while the Ru-Ti@ V_B -BN system evidently shows the largest magnetic moment. For this reason, the $\text{N}\equiv\text{N}$ triple bond of the N_2 molecule on the magnetic Ru-Ti@ V_B -BN monolayer is weakened, thus leading to stronger N_2 adsorption.

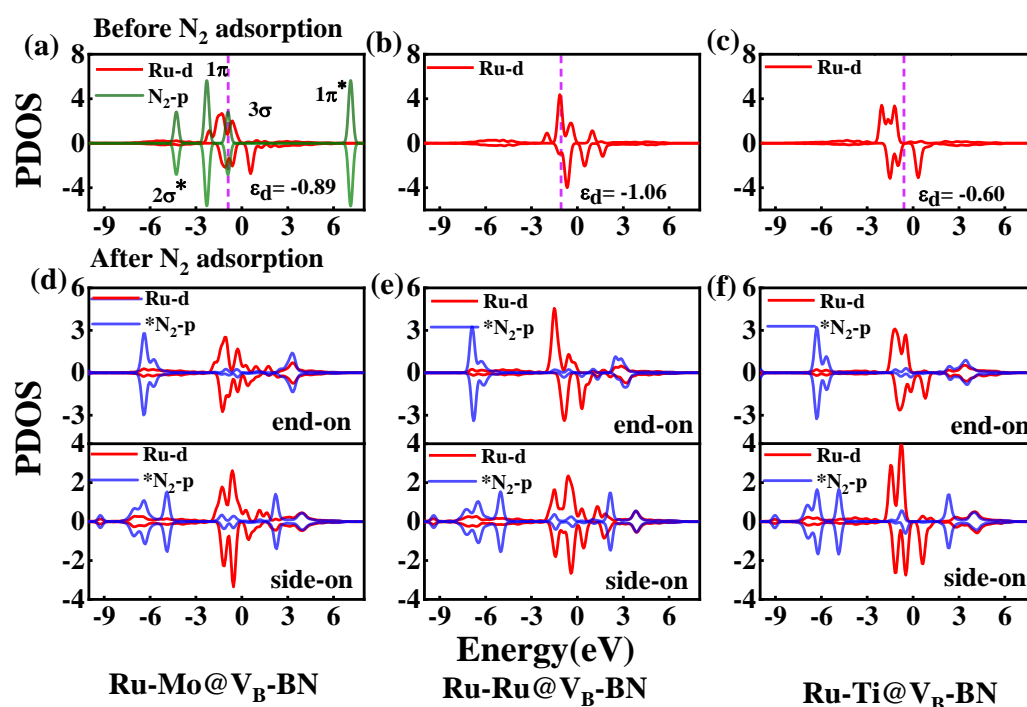


Figure 4. Partial density of states (PDOS) of (a) free N_2 molecule and Ru $4d$ orbitals in (a) Ru-Mo@ V_B -BN; (b) Ru-Ru@ V_B -BN and (c) Ru-Ti@ V_B -BN before N_2 adsorption. PDOS of N_2 p and Ru $4d$ orbitals in (d) Ru-Mo@ V_B -BN; (e) Ru-Ru@ V_B -BN and (f) Ru-Ti@ V_B -BN after N_2 adsorption in end-on (upper panel) and side-on manner (bottom panel). The purple dashed line represents the corresponding energy level of the d -band center (ε_d) of the Ru active site, and the Fermi level is set to 0 eV.

2.5. Full Conversion of N_2 to NH_3 on Ru-Mo/Ru/Ti@ V_B -BN

Based on the above discussion, we focused on three catalysts (Ru-Mo@ V_B -BN, Ru-Ru@ V_B -BN and Ru-Ti@ V_B -BN) to search for the most promising catalyst. We canvassed the full reaction path search through three possible mechanisms: distal, alternative and enzymatic mechanisms [35–37]. All of the optimized intermediates along the proposed reaction mechanisms are illustrated in Figure 5a, and their relevant ΔG values are summarized in Supplementary Tables S6–S11. As Figure 5b demonstrates, the optimal NRR mechanism for the Ru-Mo@ V_B -BN and Ru-Ru@ V_B -BN systems are both the distal mechanism, while the Ru-Ti@ V_B -BN catalyst prefers the enzymatic mechanism. Importantly, the rate-determining step (RDS) of all catalysts is the first hydrogenation process. Our calculated RDSs for Ru-Mo/Ru/Ru/Ti@ V_B -BN catalysts are 0.47, 0.54 and 0.40 eV, respectively. Apparently, Ru-Ti@ V_B -BN possesses the highest activity, with a limiting potential of -0.40 V through an enzymatic mechanism. It is worth noting that Ru-Ti@ V_B -BN exhibits comparable and even better NRR activity than most of the reported NRR SACs, such as Mo_2 @PTI (-0.53 V) [38], Ru@ Ti_3C_2 (-0.40 V) [39], Ru₂@GDY (-0.55 V) [40], Fe-MoS₂ (-1.02 V) [41] and Ti@Ru(0001) (-0.47 V) [42]. In addition, we also considered the effect of van der Waals correction. As shown in Supplementary Figure S5, the van der Waals correction has no effect on the rate-determining steps and overall reaction trend of NRR.

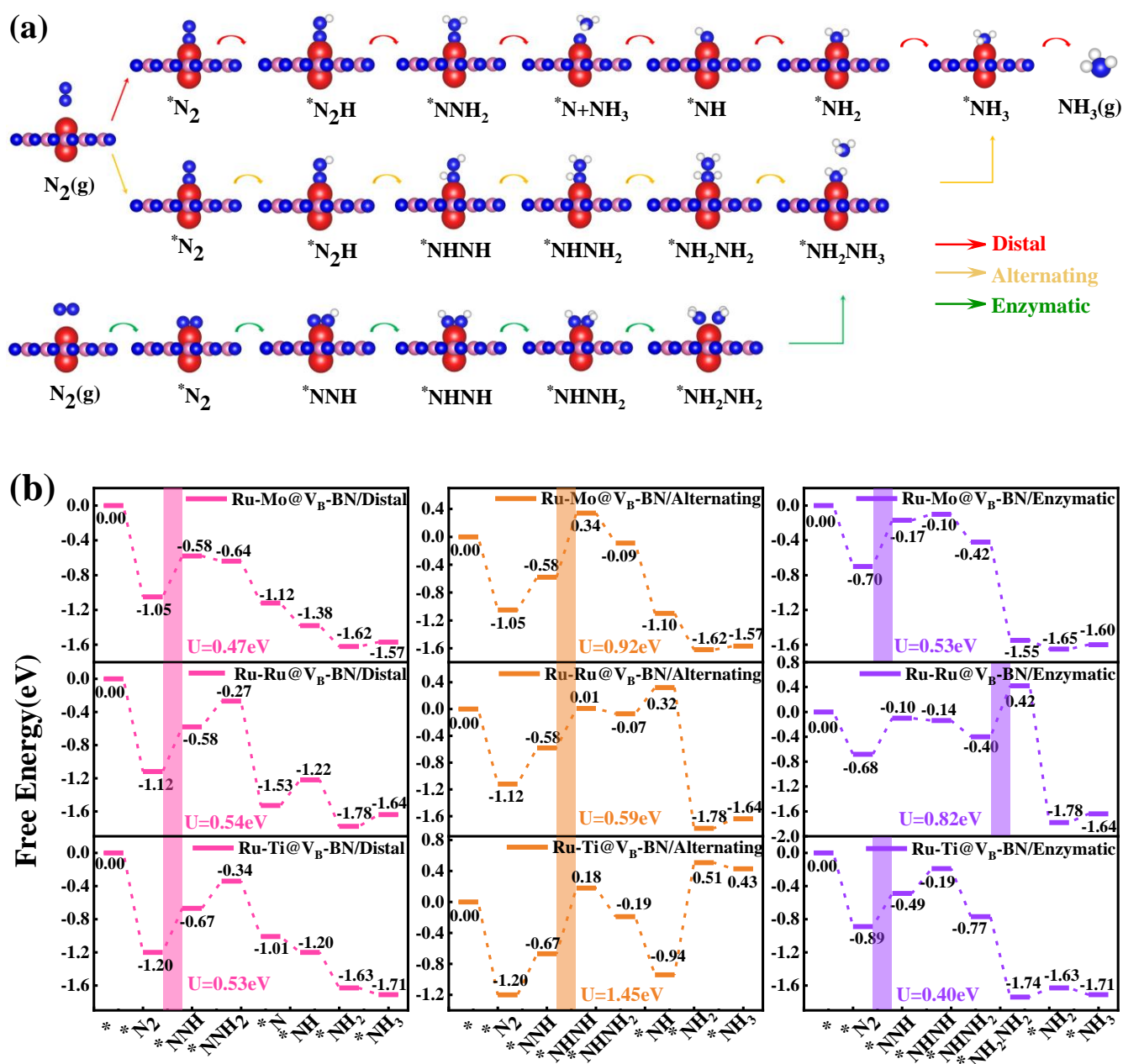


Figure 5. (a) Schematic diagram of the possible reaction mechanisms and geometry structures of the corresponding intermediate products during the NRR process. (b) Gibbs free energy diagram for NRR on Ru-Mo@ V_B -BN, Ru-Ru@ V_B -BN and Ru-Ti@ V_B -BN catalysts.

Taking the optimal Ru-Ti@ V_B -BN as an example, we further examined the evolution behaviors of the Bader charge of each intermediate along the favorable enzymatic mechanism. During the whole NRR process, each intermediate was divided into three parts, namely the defective BN monolayer, the TM dimer and the adsorbed N_xH_y species. Figure 6a shows the variations of the Bader charge of three parts, and all the data are summarized in Supplementary Table S12. The adsorbed N_xH_y and V_B -BN can gain electrons from the Ru-Ti pairs for the N_2 adsorption and the former two hydrogenation steps. Then the electrons of the adsorbed N_xH_y backflow to the Ru-Ti dimer for the $*NNH_2$ formation. In the following hydrogenation processes, N_xH_y species continue to acquire electrons from Ru-Ti, and the backflow of electrons occur until the subsequent desorption of NH_3 . Thus, the defective BN monolayer acts as an electron acceptor during NRR, while Ru-Ti pairs always reserve as the electron donors in the process of trapping the intermediates.

Furthermore, we also examined the bond-length variations of N-N, Ru-N and Ru-Ti bonds (see Figure 6b and Supplementary Table S13). Markedly, the N₂ molecule can be properly activated on Ru-Ti@V_B-BN, as is proved by the constant increase (decrease) in $d_{\text{N-N}}$ ($d_{\text{Ru-N}}$). When the first NH₃ is desorbed, $d_{\text{N-N}}$ rapidly increases, signifying the breakage of the N-N bond and practicability to generate and release the first NH₃.

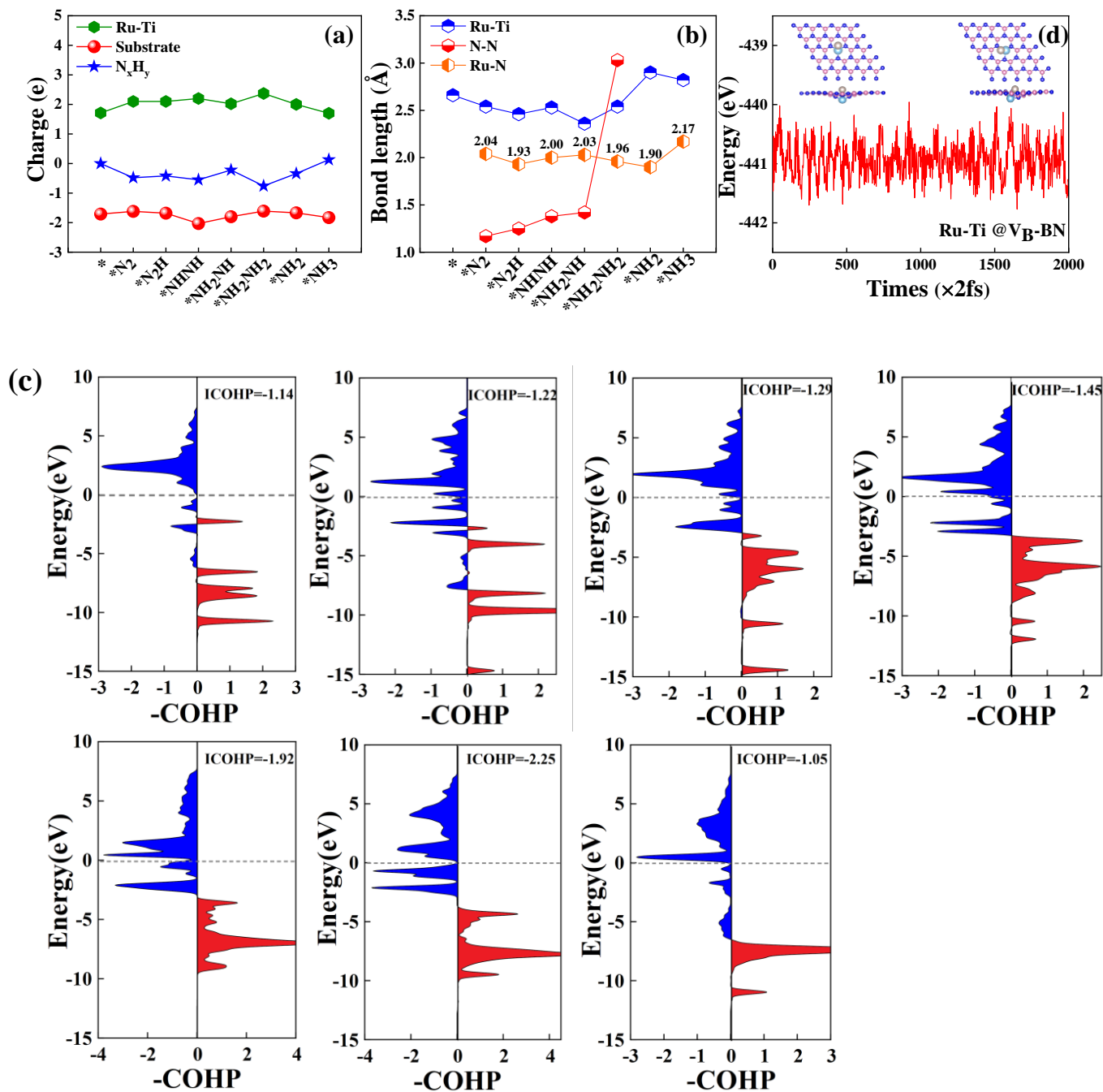


Figure 6. (a) Charge variations of defective BN monolayer, dopant TM pairs and the adsorbed N_xH_y species along the enzymatic mechanism. (b) Bond-length evolutions of N-N, Ru-N and Ru-Ti dimer. (c) Projected crystal orbital Hamilton populations (pCOHPs) between the TM and N atom in *N₂, *NNH, *NHNH, *NHNH₂, *NH₂NH₂, *NH₂ and *NH₃ on Ru-Ti@V_B-BN. (d) AIMD simulation for Ru-Ti@V_B-BN under 400 K.

We further performed the projected crystal orbital Hamiltonian population (pCOHP) analysis to illustrate the bonding-strength evolutions of the Ru-N bond for each NRR species [43]. Figure 6c shows an increased orbital interaction of the Ru-N bond as the hydrogenation step continues, and this can be confirmed by the increase of bonding contributions below the Fermi level. To gain a quantitative indicator, we calculated the integral value of COHP (ICOHP, a more negative value corresponds to a stronger TM-N interaction). The obtained ICOHP values of *N_2 , *NNH , *NHNH , *NH_2NH and *NH_2NH_2 are -1.14 , -1.22 , -1.29 , -1.45 and -1.92 , respectively, further proving the gradually strengthened Ru-N bonding. After the first *NH_3 desorbed, the bonding state of Ru-N reached the strongest interaction, with an ICOHP value of -2.25 . For *NH_3 , the ICOHP value decreased to -1.05 , indicating the weakened Ru-N bond to expedite the formation of the second NH_3 .

Afterward, the thermal stability of Ru-Ti@V_B-BN was further evaluated by AIMD simulations, under 400 K for 4 ps, with the time step of 2 fs, as shown in Figure 6d. Obviously, the total energy converges quickly, and no significant geometrical distortion occurs over the whole simulation time, implying the relatively high thermodynamic stability of Ru-Ti@V_B-BN. Ru-Ru/Mo@V_B-BN exhibits similar behaviors under the same AIMD simulation conditions (Supplementary Figure S6). On this basis, we can predict that the established Ru-Ti@V_B-BN catalyst is stable at ambient condition and holds great promise to be synthesized experimentally ahead.

3. Materials and Methods

All of the spin polarized density functional theory (DFT) calculations were performed by using the projector augmented wave (PAW) formalism and implemented in the Vienna Ab initio Simulation Package (VASP) [44,45]. Exchange-correlation potential was treated by the generalized gradient approximation (GGA) in the form of the Perdew–Bruke–Ernzerhof (PBE) functional [46]. A plane-wave basis set with an energy cutoff of 520 eV was chosen for all computations, based on our convergence test (see Supplementary Figure S1). A $(4 \times 4 \times 1)$ supercell was used to model the defective BN monolayer by removing one B atom. To avoid interactions between periodic images, a vacuum of 20 Å was set in the z direction. A Monkhorst–Pack grid of $3 \times 3 \times 1$ was used to sample the first Brillouin zones. The convergence limits for energy and force were set to 10^{-5} eV and 0.02 eV Å⁻¹, respectively. The long-range van der Waals interactions were treated by Grimme’s scheme (DFT-D3) [47]. A Bader charge analysis was carried out to account for the quantitative description of charge distribution and charge transfer. In addition, the thermodynamic stability of the catalysts was investigated by using ab initio molecular dynamics (AIMD) simulations under the NVT ensemble [48]. The AIMD calculations lasted for 4 ps, with a time step of 2.0 fs at 400 K.

The change of Gibbs free energy (ΔG) of each elementary step for NRR reaction was calculated by the following equation:

$$\Delta G = \Delta E + \Delta E_{ZPE} - T\Delta S + \Delta G_{pH} + eU$$

where ΔE denotes the reaction energy, which could be directly obtained from DFT calculations; and ΔE_{ZPE} and ΔS are zero-point energy and entropy change at 298.15 K, which are computed from the frequency analysis [49]. Moreover, ΔG_{pH} is the correction of the H⁺ free energy in the aqueous solution, which can be calculated by using the formula:

$$\Delta G_{pH} = k_B T \times \ln 10 \times pH$$

where the k_B is the Boltzmann constant and the pH is set to be zero in this work; and e and U refer to the number of electrons transferred and the applied electrode potential, respectively. The applied electrode potential of each step is defined as follows:

$$U = -\Delta G/e$$

4. Conclusions

In summary, this study locked 10 cage-like dual-atom catalysts anchored in V_B -BN and fully investigated their stability, selectivity and activity. Based on a “three-step” screening strategy, three promising NRR catalysts, namely Ru-Mo@ V_B -BN, Ru-Ru@ V_B -BN and Ru-Ti@ V_B -BN, were singled out by the density functional theory calculations. In particular, Ru-Ti@ V_B -BN was screened out as the most potential catalyst for NRR, as well as a favorable limiting potential of -0.40 V, through enzymatic mechanism. Among the Ru-Mo/Ru/Ti@ V_B -BN candidates, Ru-Ti dimer exhibits the largest magnetic moment, which remarkably activates the N_2 molecule. Compared with the corresponding SAC (Ru@ V_B -BN), Ru-Mo/Ru/Ti dimers contribute more electrons to the molecular N_2 , which also ensures a more significant activation of the inert $N\equiv N$ bond. Moreover, heteronuclear DACs (Ru-Ti/Mo) can effectively modulate the d -band center of the Ru active site better than the homonuclear DACs (Ru-Ru). Hence, Ru-Ti with a d -band center closer to the Fermi level reduces the RDS values for the first hydrogenation ($*N_2 + H^- + e^- \rightarrow *N_2H$) process, due to the highly activated N_2 molecule and enhanced adsorption of NNH^* with lower energy. We hope that the findings and insights provide theoretical guidance for the theoretical design and experimental synthesis of defective boron nitride-hosted DACs.

Supplementary Materials: The following supporting information can be downloaded at <https://www.mdpi.com/article/10.3390/catal12111404/s1>. The detailed data and figures calculated in this work: Table S1. Computed cohesive energy (E_{coh}) and adsorption energy (E_a) of TM dimer (TM = Ti, Fe, Mo and Ru) anchored on the B-vacancy. Table S2. Calculated the amount of the transferred electrons from the anchored TM atoms to the V_B -BN (Q in e) of TM_1 - TM_2 @ V_B -BN. Table S3. Calculated bond lengths of adsorbed $*N_2$ (d_{N-N} in Å) and the amount of charge that $*N_2$ gained from the TM_1 - TM_2 @ V_B -BN catalysts (Q in e). Table S4: Calculated free energy changes of the first hydrogenation step ($\Delta G_{*N_2 \rightarrow *N_2H}$) and the last hydrogenation step ($\Delta G_{*NH_2 \rightarrow *NH_3}$) for 16 TM_1 - TM_2 @ V_B -BN catalysts. “/” indicates that TM atoms cannot adsorb intermediate $*N_2H$. Table S5: The magnetic moments ($M_{\mu B}$) of TMs in TM_1 - TM_2 @ V_B -BN catalysts. Table S6: The Gibbs free energies changes for each intermediate on Ru-Mo@ V_B -BN via distal, alternating and enzymatic mechanisms at 298.15 K (in eV). Table S7: Computed vibrational frequencies, zero-point energies and entropy of reaction intermediates on Ru-Mo@ V_B -BN, where * denotes the adsorption site. Table S8: The Gibbs free energies changes for each intermediate on Ru-Ru@ V_B -BN via distal, alternating and enzymatic mechanisms at 298.15 K (in eV). Table S9: Computed vibrational frequencies, zero-point energies and entropy of reaction intermediates on Ru-Ru@ V_B -BN, where * denotes the adsorption site. Table S10: The Gibbs free energies changes for each intermediate on Ru-Ti@ V_B -BN via distal, alternating and enzymatic mechanisms at 298.15 K (in eV). Table S11: Computed vibrational frequencies, zero-point energies and entropy of reaction intermediates on Ru-Ti@ V_B -BN, where * denotes the adsorption site. Table S12: Charge variations of Ru-Ti dimer, V_B -BN substrate and N_xH_y species on Ru-Ti@ V_B -BN. Table S13: Bond lengths of Ru-Ti, N-N and Ru-N on Ru-Ti@ V_B -BN. Table S14: The calculated total energies (Energy-DFT), zero-points energy (ZPE) and entropy corrections (TS), in eV, for the gas phase N_2 , H_2 , NH_3 species of NRR ($T = 298.15$ K, $P = 1$ bar). In comparison, the experimental entropies (TS_{exp}) of the gas phase N_2 , H_2 , NH_3 species are also shown, which are from NIST standard reference database. Figure S1. Convergence test on the ENCUT value for the BN primitive cell. Figure S2. Schematic diagrams of the fully relaxed structures of TM_1 - TM_2 @ V_B -BN (TM = Fe, Mo, Ru and Ti). Figure S3. Top and side views of N_2 molecule adsorbed on a single Ru atom in (a) end-on and (b) side-on configuration, respectively. Change density differences of N_2 adsorption on Ru@ V_B -BN monolayer for (c) end-on and (d) side-on configurations. Figure S4. Projected density of states (PDOS) of Ru d orbitals in Ru@ V_B -BN. The red dotted line represents the position of the d -band center. Figure S5. Gibbs free energy diagram for N_2 electroreduction on Ru-Ti@ V_B -BN with and without consideration of vdW interaction. Figure S6. Variations of the total energy against the time for the AIMD simulation for Ru-Mo @ V_B -BN and Ru-Ru @ V_B -BN under 400 K.

Author Contributions: Writing—original draft preparation and calculations, R.C.; visualization, J.-Z.X.; writing—review and editing, Q.W. All authors have read and agreed to the published version of the manuscript.

Funding: This work was financially supported by the National Natural Science Foundation of China (Grant No. 22168036), Department of Education of Tibet Autonomous Region ([2021]1-21), the Central Government Funds for Local Science and Technological Development (No. XZ202201YD0020C), and Tibet University Postgraduate Students' High-Level Talent Training Plan Project (No. 2020-GSP-S039, 2020-GSP-S040).

Data Availability Statement: Not applicable.

Conflicts of Interest: The authors declare no conflict of interest.

References

1. Montoya, J.H.; Tsai, C.; Vojvodic, A.; Nørskov, J.K. The challenge of electrochemical ammonia synthesis: A new perspective on the role of nitrogen scaling relations. *ChemSusChem* **2015**, *8*, 2180–2186. [[CrossRef](#)]
2. Licht, S.; Cui, B.; Wang, B.; Li, F.; Lau, J.; Liu, S. Ammonia synthesis by N₂ and steam electrolysis in molten hydroxide suspensions of nanoscale Fe₂O₃. *Science* **2014**, *345*, 637–640. [[CrossRef](#)]
3. Suryanto, B.H.; Matuszek, K.; Choi, J.; Hodgetts, R.Y.; Du, H.; Bakker, J.M.; Kang, C.S.; Cherepanov, P.V.; Simonov, A.N.; MacFarlane, D.R. Nitrogen reduction to ammonia at high efficiency and rates based on a phosphonium proton shuttle. *Science* **2021**, *372*, 1187–1191. [[CrossRef](#)]
4. MacFarlane, D.R.; Cherepanov, P.V.; Choi, J.; Suryanto, B.H.; Hodgetts, R.Y.; Bakker, J.M.; Vallana, F.M.F.; Simonov, A.N. A roadmap to the ammonia economy. *Joule* **2020**, *4*, 1186–1205. [[CrossRef](#)]
5. Soloveichik, G. Electrochemical synthesis of ammonia as a potential alternative to the Haber–Bosch process. *Nat. Catal.* **2019**, *2*, 377–380. [[CrossRef](#)]
6. Yao, Y.; Wang, H.; Yuan, X.; Li, H.; Shao, M. Electrochemical nitrogen reduction reaction on ruthenium. *ACS Energy Lett.* **2019**, *4*, 1336–1341. [[CrossRef](#)]
7. Rohr, B.A.; Singh, A.R.; Nørskov, J.K. A theoretical explanation of the effect of oxygen poisoning on industrial Haber-Bosch catalysts. *J. Catal.* **2019**, *372*, 33–38. [[CrossRef](#)]
8. Martín, A.J.; Pérez-Ramírez, J. Heading to distributed electrocatalytic conversion of small abundant molecules into fuels, chemicals, and fertilizers. *Joule* **2019**, *3*, 2602–2621. [[CrossRef](#)]
9. Yan, Z.; Ji, M.; Xia, J.; Zhu, H. Nitrogen reduction reaction: Recent advanced materials for electrochemical and photoelectrochemical synthesis of ammonia from dinitrogen: One step closer to a sustainable energy future. *Adv. Energy Mater.* **2020**, *10*, 2070049. [[CrossRef](#)]
10. Guo, X.; Du, H.; Qu, F.; Li, J. Recent progress in electrocatalytic nitrogen reduction. *J. Mater. Chem. A* **2019**, *7*, 3531–3543. [[CrossRef](#)]
11. Wang, D.; Azofra, L.M.; Harb, M.; Cavallo, L.; Zhang, X.; Suryanto, B.H.; MacFarlane, D.R. Energy-efficient nitrogen reduction to ammonia at low overpotential in aqueous electrolyte under ambient conditions. *ChemSusChem* **2018**, *11*, 3416–3422. [[CrossRef](#)]
12. Singh, A.R.; Rohr, B.A.; Statt, M.J.; Schwalbe, J.A.; Cargnello, M.; Nørskov, J.K. Strategies toward selective electrochemical ammonia synthesis. *ACS Catal.* **2019**, *9*, 8316–8324. [[CrossRef](#)]
13. Wang, X.; Zhang, Q.; Hao, W.; Fang, C.; Zhou, J.; Xu, J. A novel porous graphitic carbon nitride (g-C₇N₃) substrate: Prediction of metal-based π -d conjugated nanosheets toward the highly active and selective electrocatalytic nitrogen reduction reaction. *J. Mater. Chem. A* **2022**, *10*, 15036–15050. [[CrossRef](#)]
14. Hu, X.; Xiong, L.; Fang, W.-H.; Su, N.Q. Computational insight into metallated graphynes as single atom electrocatalysts for nitrogen fixation. *ACS Appl. Mater. Interfaces* **2022**, *14*, 27861–27872. [[CrossRef](#)]
15. Wu, Y.; He, C.; Zhang, W. “Capture-backdonation-recapture” mechanism for promoting N₂ reduction by heteronuclear metal-free double-atom catalysts. *J. Am. Chem. Soc.* **2022**, *44*, 9344–9353. [[CrossRef](#)]
16. Chen, Z.W.; Yan, J.M.; Jiang, Q. Single or double: Which is the altar of atomic catalysts for nitrogen reduction reaction? *Small Methods* **2019**, *3*, 1800291. [[CrossRef](#)]
17. Zhang, Z.; Huang, X.; Xu, H. Anchoring an Fe dimer on nitrogen-doped graphene toward highly efficient electrocatalytic ammonia synthesis. *ACS Appl. Mater. Interfaces* **2021**, *13*, 43632–43640. [[CrossRef](#)]
18. Ma, Z.; Cui, Z.; Xiao, C.; Dai, W.; Lv, Y.; Li, Q.; Sa, R. Theoretical screening of efficient single-atom catalysts for nitrogen fixation based on a defective BN monolayer. *Nanoscale* **2020**, *12*, 1541–1550. [[CrossRef](#)]
19. Jin, C.; Lin, F.; Suenaga, K.; Iijima, S. Fabrication of a freestanding boron nitride single layer and its defect assignments. *Phys. Rev. Lett.* **2009**, *102*, 195505. [[CrossRef](#)]
20. Hong, J.; Jin, C.; Yuan, J.; Zhang, Z. Atomic defects in two-dimensional materials: From single-atom spectroscopy to functionalities in opto-/electronics, nanomagnetism, and catalysis. *Adv. Mater.* **2017**, *29*, 1606434. [[CrossRef](#)]
21. Zhao, J.; Chen, Z. Single Mo atom supported on defective boron nitride monolayer as an efficient electrocatalyst for nitrogen fixation: A computational study. *J. Am. Chem. Soc.* **2017**, *139*, 12480–12487. [[CrossRef](#)] [[PubMed](#)]
22. Zou, Y.; Wen, L.; Bian, X.; Zhang, Y.; Lin, W.; Huang, S.; Ding, K. Fe, Mo-Co-doped graphene for electrocatalytic N₂-to-NH₃ conversion: A DFT investigation. *Appl. Surf. Sci.* **2021**, *569*, 150921. [[CrossRef](#)]
23. Yang, W.; Huang, H.; Ding, X.; Ding, Z.; Wu, C.; Gates, I.D.; Gao, Z. Theoretical study on double-atom catalysts supported with graphene for electroreduction of nitrogen into ammonia. *Electrochim. Acta* **2020**, *335*, 135667. [[CrossRef](#)]

24. He, T.; Santiago, A.R.P.; Du, A. Atomically embedded asymmetrical dual-metal dimers on N-doped graphene for ultra-efficient nitrogen reduction reaction. *J. Catal.* **2020**, *388*, 77–83. [[CrossRef](#)]
25. Zhao, W.; Chen, L.; Zhang, W.; Yang, J. Single Mo1 (W1, Re1) atoms anchored in pyrrolic-N3 doped graphene as efficient electrocatalysts for the nitrogen reduction reaction. *J. Mater. Chem. A* **2021**, *9*, 6547–6554. [[CrossRef](#)]
26. Hellman, A.; Honkala, K.; Remediakis, I.; Logadottir, A.; Carlsson, A.; Dahl, S.; Christensen, C.H.; Nørskov, J.K. Ammonia synthesis and decomposition on a Ru-based catalyst modeled by first-principles. *Surf. Sci.* **2009**, *603*, 1731–1739. [[CrossRef](#)]
27. Ghuman, K.K.; Tozaki, K.; Sadakiyo, M.; Kitano, S.; Oyabe, T.; Yamauchi, M. Tailoring widely used ammonia synthesis catalysts for H and N poisoning resistance. *Phys. Chem. Chem. Phys.* **2019**, *21*, 5117–5122. [[CrossRef](#)]
28. Wang, Y.; Du, Y.; Meng, Y.; Xie, B.; Ni, Z.; Xia, S. Monatomic Ti doped on defective monolayer boron nitride as an electrocatalyst for the synthesis of ammonia: A DFT study. *Appl. Surf. Sci.* **2021**, *563*, 150277. [[CrossRef](#)]
29. Chen, Y.; Zhang, X.; Qin, J.; Liu, R. High-throughput screening of single metal atom anchored on N-doped boron phosphide for N₂ reduction. *Nanoscale* **2021**, *13*, 13437–13450. [[CrossRef](#)]
30. Huang, B.; Wu, Y.; Chen, B.; Qian, Y.; Zhou, N.; Li, N. Transition-metal-atom-pairs deposited on g-CN monolayer for nitrogen reduction reaction: Density functional theory calculations. *Chin. J. Catal.* **2021**, *42*, 1160–1167. [[CrossRef](#)]
31. Choi, C.; Back, S.; Kim, N.-Y.; Lim, J.; Kim, Y.-H.; Jung, Y. Suppression of hydrogen evolution reaction in electrochemical N₂ reduction using single-atom catalysts: A computational guideline. *ACS Catal.* **2018**, *8*, 7517–7525. [[CrossRef](#)]
32. Singh, A.R.; Rohr, B.A.; Schwalbe, J.A.; Cargnello, M.; Chan, K.; Jaramillo, T.F.; Chorkendorff, I.; Nørskov, J.K. Electrochemical ammonia synthesis the selectivity challenge. *ACS Publ.* **2017**, *7*, 706–709. [[CrossRef](#)]
33. Azofra, L.M.; Sun, C.; Cavallo, L.; MacFarlane, D.R. Feasibility of N₂ binding and reduction to ammonia on Fe-deposited MoS₂ 2d sheets: A DFT study. *Chem. Eur. J.* **2017**, *23*, 8275–8279. [[CrossRef](#)] [[PubMed](#)]
34. Guo, X.; Huang, S. Tuning nitrogen reduction reaction activity via controllable Fe magnetic moment: A computational study of single Fe atom supported on defective graphene. *Electrochim. Acta* **2018**, *284*, 392–399. [[CrossRef](#)]
35. Wang, C.; Zhao, Y.; Zhu, C.; Zhang, M.; Geng, Y.; Li, Y.; Su, Z. A two-dimensional conductive Mo-based covalent organic framework as an efficient electrocatalyst for nitrogen fixation. *J. Mater. Chem. A* **2020**, *8*, 23599–23606. [[CrossRef](#)]
36. Seefeldt, L.C.; Hoffman, B.M.; Dean, D.R. Mechanism of Mo-dependent nitrogenase. *Annu. Rev. Biochem.* **2009**, *78*, 701. [[CrossRef](#)]
37. Hinnemann, B.; Nørskov, J.K. Catalysis by enzymes: The biological ammonia synthesis. *Top. Catal.* **2006**, *37*, 55–70. [[CrossRef](#)]
38. Le, Y.; Wei, C.; Xue, W.; Li, Y.; Zhang, Y.; Lin, W. Nitrogen reduction on crystalline carbon nitride supported by homonuclear bimetallic atoms. *J. Chem. Phys.* **2022**, *157*, 114704. [[CrossRef](#)]
39. Liu, A.; Gao, M.; Ren, X.; Meng, F.; Yang, Y.; Yang, Q.; Guan, W.; Gao, L.; Liang, X.; Ma, T. A two-dimensional Ru@Mxene catalyst for highly selective ambient electrocatalytic nitrogen reduction. *Nanoscale* **2020**, *12*, 10933–10938. [[CrossRef](#)]
40. Hu, L.G.; Wang, H.J.; Su, Y. Computational study of double transition metal atom anchored on graphdiyne monolayer for nitrogen electroreduction. *ChemPhysChem* **2022**, *23*, e202200149. [[CrossRef](#)]
41. Azofra, L.M.; Li, N.; MacFarlane, D.R.; Sun, C. Promising prospects for 2d d₂–d₄ M₃C₂ transition metal carbides (Mxenes) in N₂ capture and conversion into ammonia. *Energy Environ. Sci.* **2016**, *9*, 2545–2549. [[CrossRef](#)]
42. Kour, G.; Mao, X.; Du, A. Computational screening of single-atom alloys TM@Ru(0001) for enhanced electrochemical nitrogen reduction reaction. *J. Mater. Chem. A* **2022**, *10*, 6204–6215. [[CrossRef](#)]
43. Dronskowski, R.; Blochl, P.E. Crystal orbital hamilton populations (cohp)—Energy-resolved visualization of chemical bonding in solids based on density-functional calculations. *J. Phys. Chem.* **1993**, *97*, 8617–8624. [[CrossRef](#)]
44. Kresse, G.; Furthmüller, J. Efficient iterative schemes for ab initio total-energy calculations using a plane-wave basis set. *Phys. Rev. B* **1996**, *54*, 11169. [[CrossRef](#)]
45. Kresse, G.; Joubert, D. From ultrasoft pseudopotentials to the projector augmented-wave method. *Phys. Rev. B* **1999**, *59*, 1758. [[CrossRef](#)]
46. Perdew, J.P.; Ernzerhof, M.; Burke, K. Rationale for mixing exact exchange with density functional approximations. *J. Chem. Phys.* **1996**, *105*, 9982–9985. [[CrossRef](#)]
47. Grimme, S.; Antony, J.; Ehrlich, S.; Krieg, H. A consistent and accurate ab initio parametrization of density functional dispersion correction (DFT-d) for the 94 elements h-Pu. *J. Chem. Phys.* **2010**, *132*, 154104. [[CrossRef](#)]
48. Tuckerman, M.; Laasonen, K.; Sprik, M.; Parrinello, M. Ab initio molecular dynamics simulation of the solvation and transport of hydronium and hydroxyl ions in water. *J. Chem. Phys.* **1995**, *103*, 150–161. [[CrossRef](#)]
49. Nørskov, J.K.; Rossmeisl, J.; Logadottir, A.; Lindqvist, L.; Kitchin, J.R.; Bligaard, T.; Jonsson, H. Origin of the overpotential for oxygen reduction at a fuel-cell cathode. *J. Phys. Chem. B* **2004**, *108*, 17886–17892. [[CrossRef](#)]